Strongly asymmetric wavelength dependence of optical gain in nanocavity-based Raman silicon lasers

Research Article Vol. 5, No. 10 / October 2018 / Optica 1256

Strongly asymmetric wavelength dependence of optical gain in nanocavity-based Raman silicon lasers

Daiki Yamashita,[1,*] Takashi Asano,[2] Susumu Noda,[2,3] and Yasushi Takahashi[1]

[1]Department of Physics and Electronics, Osaka Prefecture University, Sakai, Osaka 599-8531, Japan
[2]Department of Electronic Science and Engineering, Kyoto University, Kyoto 615-8510, Japan
[3]Photonics and Electronics Science and Engineering Center, Kyoto University, Kyoto 615-8510, Japan
*Corresponding author: d-yamashita@pe.osakafu-u.ac.jp

Received 10 July 2018; revised 12 September 2018; accepted 14 September 2018 (Doc. ID 338250); published 9 October 2018

While the realization of silicon lasers using interband transitions is still technically problematic, utilization of Raman scattering processes seems to be the most feasible alternative. Raman silicon lasers based on photonic crystal nanocavities provide sub-microwatt thresholds and CMOS compatibility. Therefore, this type of laser is suitable for dense integration in Si photonic circuits. However, details of the gain mechanism, which are important for improving laser performance, have rarely been discussed due to the lack of a suitable characterization technique. Here, we report on the excitation-wavelength dependence of optical gain in a high-quality nanocavity-based Raman silicon laser. For this, we employ a so-called stimulated-Raman-scattering excitation (SRE) spectroscopy, which allows us to reveal the range of excitation wavelengths enabling laser operation, the excitation condition for maximum output, shift of the gain peak, and enhancement of Raman gain including nonlinear optical losses. In particular, we find that laser output remarkably decreases in the long-wavelength region of cavity resonance as excitation power increases. Numerical simulations suggest that optical loss due to free-carrier absorption induced by two-photon absorption grows substantially above a certain threshold.

https://doi.org/10.1364/OPTICA.5.001256

1. INTRODUCTION

Although silicon (Si) is used for many different types of electronic devices, its indirect bandgap is problematic for certain applications. For example, due to the resulting low radiative efficiency of the electron–hole recombination, optical gain is weak. Consequently, the realization of Si-based lasers using interband transitions has proven to be very difficult [1,2]. To solve the problem of the lack in optical gain, use of stimulated Raman scattering (SRS) in bulk crystalline Si has been proposed because Si has a large Raman gain coefficient and transparency for optical communication bands in the near infrared [3–12]. The SRS concept has been successfully implemented in optically pumped Si lasers and enabled continuous-wave (cw) operation at room temperature [13,14]. We have developed a Raman Si laser based on a photonic-crystal (PC) nanocavity to significantly lower laser threshold power [15–17]. Such nanocavities have a very compact resonator size and can be fabricated with high-quality (high-Q) factors. These features enable ultralow thresholds (microwatt or even submicrowatt [12,15,18]) and make these devices suitable for the dense integration of Si lasers in Si photonic circuits. Mass production of high-Q nanocavities using CMOS process technologies has been demonstrated recently [19,20].

In order to improve the performance of semiconductor lasers by lowering the threshold or increasing output power and energy efficiency, it is important to clarify the spectral shape of the optical gain. For example, in the early stages of research on quantum-dot lasers, quantum-wire lasers, and indium gallium nitride lasers, wavelength dependence of optical gain has been measured using several techniques, such as photoluminescence excitation (PLE) spectroscopy [21–24], the variable stripe length (VSL) method [25,26], and Hakki–Paoli method [27–29]. Unlike usual semiconductor lasers that employ interband transitions, nanocavity-based Raman Si lasers utilize two high-Q resonant modes to confine the pump light and Stokes Raman light into the cavity. These two modes have an energy separation of about 15.6 THz, which equals the Raman shift of Si [17]. Therefore, gain measurement techniques developed for traditional semiconductor lasers cannot be applied to Raman Si lasers.

It is important to note that the spectral shape of optical gain in nanocavity-based Raman Si lasers is likely to exhibit non-trivial features because two-photon absorption (TPA) is easily enhanced in high-Q nanocavities [30–33]. Carriers generated by TPA cause various detrimental effects for laser performance via free-carrier absorption (FCA), the thermo-optic effect, and the carrier plasma effect [18,34–37]. They are responsible for saturation of the gain and dynamical wavelength shifts of the two nanocavity modes. Such dynamical shifts actually strongly influence laser performance [18]. Therefore, it is important to develop a suitable measurement technique that allows us to study optical gain of Raman Si lasers based on high-Q and small-sized cavities.

In this work, we report on the excitation-wavelength dependence of optical gain in a nanocavity-based Raman Si laser studied by a so-called stimulated-Raman-scattering excitation (SRE) spectroscopy. This SRE spectroscopy is an analog of the well-established PLE spectroscopy. Here, intensity of the Stokes Raman emission from the high-Q nanocavity mode is measured as a function of excitation wavelength (in contrast to PLE, which measures interband photoluminescence from the band edge instead). We investigate SRE spectra for excitation powers (P_{input}) ranging from 0.4 to 12 times the threshold excitation power (P_{th}) in order to clarify a number of essential properties of the gain. For $P_{\mathrm{input}} < P_{\mathrm{th}}$, the spectral width of the SRE spectrum gradually decreases for increasing P_{input}, and peak intensity nonlinearly increases because the dominant mechanism contributing to Raman emission gradually changes from spontaneous Raman scattering to SRS. When P_{input} exceeds P_{th}, the excitation wavelength region capable of lasing expands, and the SRE peak red shifts due to the thermo-optic effect. The strongest laser emission is obtained at $P_{\mathrm{input}} = 2.5 \times P_{\mathrm{th}}$. Above $4.0 \times P_{\mathrm{th}}$, an unknown phenomenon is observed. Here, laser output remarkably decreases in the long-wavelength region of cavity resonance as excitation power increases. Numerical simulations suggest that this phenomenon is a result of an increase in carrier lifetime, which is accompanied by a substantially enhanced FCA loss induced by TPA.

2. SAMPLE STRUCTURE AND FUNDAMENTAL PROPERTIES

Figure 1(a) shows a schematic of the heterostructure nanocavity utilized for the Raman laser. The PC consists of a triangular lattice of circular air holes with a lattice constant (a) of 410 nm. The lattice constant in the x direction is increased symmetrically by 5 nm every two periods, with the largest a being 420 nm at the center [38]. This structure forms two confined propagation bands with lower resonance frequencies in the center, as shown in Fig. 1(b). These bands constitute the two high-Q nanocavity modes that can be used for Raman lasing. We utilized the nanocavity mode arising from the second propagation band [Fig. 1(b); light blue area] to confine the pump laser light, while the nanocavity mode arising from the first propagation band [Fig. 1(b); light red area] was used to confine the Stokes Raman scattered light. These two modes will hereafter be referred to as the pump mode and Stokes mode, respectively. The theoretical Q for the pump mode ($Q_{p,\mathrm{theory}}$) is 540,000, and that for the Stokes mode ($Q_{S,\mathrm{theory}}$) is 5,500,000 (calculated using three-dimensional finite-difference time-domain simulations).

The Raman laser is fabricated on a (100) Si-on-insulator (SOI) substrate (Soitec) with a top Si layer thickness of 220 nm and a buried-oxide (BOX) layer thickness of 3 μm. After defining the PC pattern on the resist mask by electron beam lithography, the pattern is transferred to the top Si slab through an inductively coupled plasma etching process using SF_6-based gas. The sample surface is cleaned by standard cleaning processes for Si wafers and the BOX layer underneath the PC slab is removed with hydrofluoric acid (48%, without surface active agent) to form an air-bridge structure. In order to enhance Raman gain, the x direction of the nanocavity is chosen along the [100] crystalline direction of the substrate [16]. The air–hole radius is set to about 130 nm, resulting in frequency spacing (Δf) between the two modes close to the Raman shift of the Si nanocavity, 15.606 THz [17]. Details

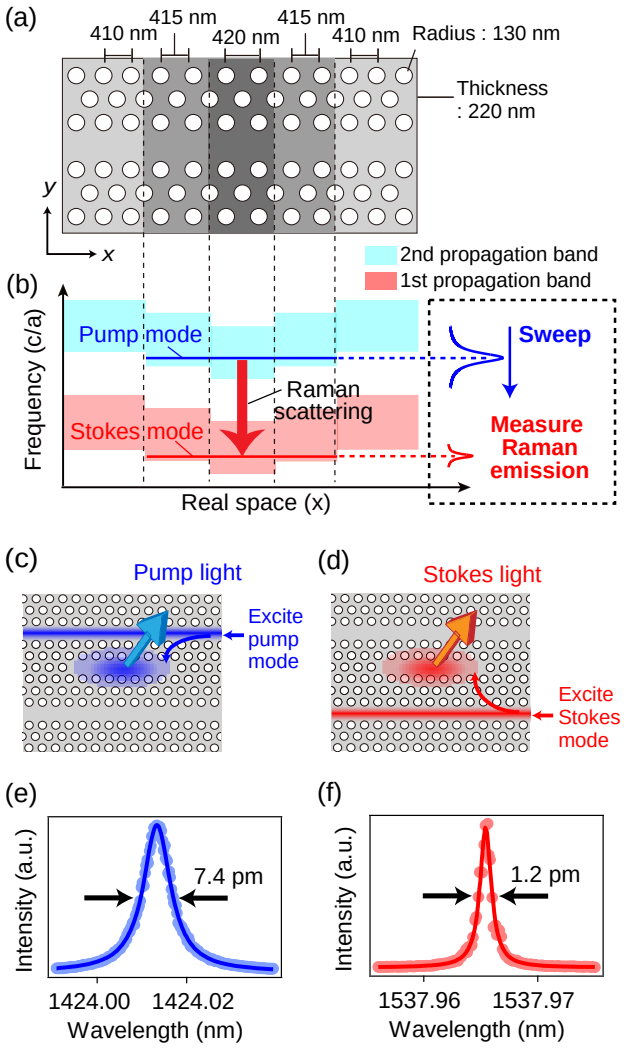

Fig. 1. (a) Schematic of the heterostructure nanocavity used for the Raman laser. (b) Band diagram of the nanocavity. The pump and Stokes nanocavity modes form through confinement in the two propagation bands. The inset on the right side of the graph outlines the SRE measurement procedure. (c) Nanocavity excitation configuration to measure properties of the pump mode, and (d) those of the Stokes mode. (e) Resonant spectrum of the pump mode, and (f) that of the Stokes mode. Filled circles show experimental data and solid lines are fitting results using a Lorentzian function.

of nanocavity design and fabrication procedure can be found in our previous paper [15].

The sample used in this study additionally contains two excitation waveguides fabricated parallel to the cavity. As shown in Fig. 1(c), the pump nanocavity mode is excited through the pump excitation waveguide via an external tunable laser, and the light emitted from the cavity in the direction vertical to the slab is measured (experimental setup is shown in Fig. 2). The illustration in Fig. 1(d) corresponds to the measurement configuration for the Stokes mode, which is excited through the Stokes excitation waveguide at lower energies. Figures 1(e) and 1(f) show experimentally obtained resonant emission spectra at weak excitation for the pump mode and the Stokes mode, respectively. Here, the excitation power is chosen sufficiently low ($0.05 \times P_{\mathrm{th}}$) to avoid influences from TPA. The Q value including the load of the excitation waveguide can be estimated from the resonance wavelength (λ) and the full width at half-maximum, FWHM ($\Delta\lambda$),

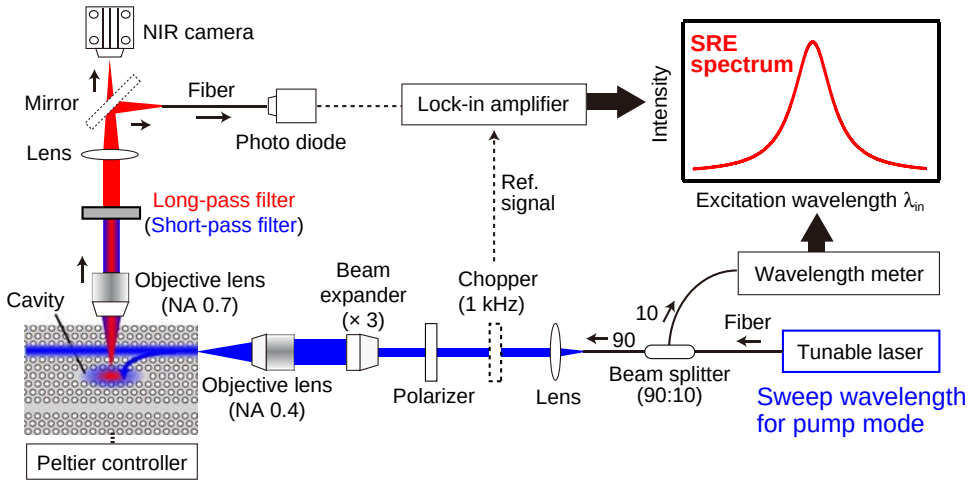

Fig. 2. Setup used to measure excitation-wavelength dependence of the pump mode light and Stokes mode light.

according to the definition $Q = \lambda/\Delta\lambda$. Q values for the pump mode (Q_p) and for Stokes mode (Q_S) estimated from Figs. 1(e) and 1(f) are 192,000 and 1,290,000, respectively, which are denoted as $Q_{p,0}$ and $Q_{S,0}$, since they represent intrinsic Q_p and Q_S values without influences from TPA. The peak wavelength of pump mode resonance (λ_p) is 1424.013 nm, and the corresponding FWHM $\Delta\lambda_p$ is 7.4 pm. We define these intrinsic values as $\lambda_{p,0}$ and $\Delta\lambda_{p,0}$, respectively. The Δf between the two modes is 15.594 THz.

$Q_{p,0}$ and $Q_{S,0}$ are lower than corresponding $Q_{p,\text{theory}}$ and $Q_{S,\text{theory}}$ values because of imperfections in the fabricated cavities. We have reported that the main sources of the Q-value reduction are scattering losses ($1/Q_{\text{scat}}$) due to structural imperfections of the air–hole geometry and absorption losses ($1/Q_{\text{abs}}$) related to the surface [39–42]. By using these two definitions for optical losses, we can represent the $Q_{i,0}(i = p, S)$ as

$$\frac{1}{Q_{i,0}} = \frac{1}{Q_{i,\text{theory}}} + \frac{1}{Q_{i,\text{scat}}} + \frac{1}{Q_{i,\text{abs}}}. \tag{1}$$

Supposing that $1/Q_{i,\text{abs}}$ is 1.25×10^{-7}, we can estimate $1/Q_{p,\text{scat}} = 3.23 \times 10^{-6}$ and $1/Q_{S,\text{scat}} = 4.68 \times 10^{-7}$. It is noted that scattering loss for the pump mode is much larger than that for the Stokes mode, which indicates that the pump mode is more sensitive to air–hole variations. The reason for this characteristic behavior is the different electric field distribution of the two modes.

3. EXPERIMENTAL SETUP

Figure 2 shows the experimental setup for the SRE spectroscopy. The light from a tunable cw laser (SANTEC, TSL-510), whose wavelength crossed $\lambda_{p,0}$ while sweeping from short to long wavelengths, was divided into two beams with a beam splitter. The weaker beam (10%) was analyzed by a high-resolution wavelength meter (Agilent 86122A). The stronger beam (90%) was modulated by a mechanical chopper with frequency of about 1 kHz and a duty ratio of 50%. Beam size was expanded with a beam expander to fill the pupil diameter of the 0.4-numerical aperture (NA) objective lens, which was used to focus the light on the facet of the pump excitation waveguide with transverse-electric polarization. The sample was placed on a high-precision six-axis stage, and sample temperature was stabilized at 297 K with a controlled Peltier element. The position of the sample was adjusted in order to couple the excitation laser light efficiently into the pump waveguide. The experiment was performed in ambient air with a relative humidity of 30%.

When the pump mode is strongly excited, Raman scattered light is emitted from the cavity via the Stokes mode in the direction vertical to the slab (Raman scattering spectra for various P_{input} are provided in Section S1 of Supplement 1). Stokes emission for the SRE spectra is measured by inserting a long-pass filter with a cutoff wavelength of 1500 nm to suppress the signal from the pump mode, which is emitted simultaneously. The optical density of the filter below 1500 nm is larger than six. On the other hand, a short-pass filter is used to measure pump emission. Emissions from the cavity are collected by a 0.7-NA objective lens placed on a three-axis stage. The position of the lens is adjusted by using a near-infrared (NIR) camera (FLIR SC2500) to project the emitted light exactly on the InGaAs photodiode. Intensities of the emitted light are measured with a lock-in amplifier system (NF Corporation LI5630) as a function of excitation wavelength (λ_{in}). The plot on the right upper side in Fig. 2 schematically shows the concept of the SRE spectrum, which plots the intensity of Stokes emission versus λ_{in}. We also measure the intensity of pump emission versus λ_{in} under the same condition for comparison (this allows us to investigate the gain mechanisms in detail).

It is important to note that a robust SRE measurement requires stable excitation of the pump mode. Although we stabilize the sample temperature using a Peltier controller, the temperature randomly varies during the measurements at least by 0.01 K, which induces a shift of ≈0.8 pm for λ_p. Therefore, $Q_{p,0}$ should not be too high, e.g., $Q_{p,0} < 300,000$ is desirable. On the other hand, the value of $Q_{S,0}$ does not affect the robustness if Δf matches the Raman shift of Si. Compared to other approaches for studying the wavelength dependence of optical gain as explained in the Introduction (PLE, VSL, and Hakki–Paoli), the advantage of SRE spectroscopy is that it can be applied in cases of excitation powers much higher than the lasing threshold. Additionally, a high signal-to-noise ratio and good wavelength resolution can be realized. On the other hand, it is not suitable for low excitation powers because emission intensity of the spontaneous Raman scattering is very weak and the absolute values of gain coefficients are unfortunately not obtained in SRE measurements.

4. EXPERIMENTAL RESULTS

A. SRE Spectra for Various Excitation Powers

Figure 3(a) shows several resonance spectra of the pump mode (blue curves) obtained for P_{input} less than $1.2 \times P_{\text{th}}$ and also corresponding SRE spectra (red curves). The horizontal axis is the excitation wavelength λ_{in}. The red numbers on the right side of the SRE spectra [Fig. 3(a); ×1, ×5, ×617] represent the scaling factors for Stokes emission intensity (emission intensity of the pump mode is almost proportional to excitation power). The excitation laser wavelength is changed in steps of ≈0.2 pm. For a low P_{input} of $0.02 \times P_{\text{th}}$, the resonance spectrum of the pump mode exhibits a symmetrical shape. There is no signal in the corresponding SRE spectrum because the Raman emission is too weak to be detected by the present setup. Typically, the efficiency of spontaneous Raman scattering is $\sim 10^{-5}$ even in Raman Si nanocavity lasers [15]. For a P_{input} of $0.4 \times P_{\text{th}}$, λ_p slightly red shifts, and the spectral shape becomes asymmetric because carriers generated by TPA cause a refractive index shift, mainly through the thermo-optic effect and carrier plasma effect [18,31–33]. The influence of the thermal effect is larger than the plasma effect and thus the resonant peak exhibits a red shift [18,31,33]. Here, the shape of the SRE spectrum almost agrees with that of the pump spectrum. This indicates that Stokes emission mainly originates from spontaneous Raman scattering. Under $P_{\text{input}} = 0.8 \times P_{\text{th}}$, the FWHM of the SRE spectrum ($\Delta\lambda_{\text{SRE}}$) becomes narrower than the $\Delta\lambda_p$, and, in addition, SRE intensity nonlinearly increases. This indicates that the SRS starts to govern Raman emission. At $P_{\text{input}} = 1.2 \times P_{\text{th}}$, SRE intensity is 120 times larger than that for $0.8 \times P_{\text{th}}$. The $\Delta\lambda_{\text{SRE}}$ is half of $\Delta\lambda_{p,0}$ (7.4 pm), since the SRE spectrum originates mainly from Raman lasing emission. As we increase P_{input}, the asymmetry of the pump spectrum and the $\Delta\lambda_p$ gradually increase, and λ_p continues to red shift. These behaviors of the pump mode are the same as those reported for high-Q Si nanocavities [31–33]. The observed behavior of the SRE spectrum in this excitation regime is as expected, and it is noted that the SRE peak wavelength (λ_{SRE}) also red shifts and almost coincides with λ_p. Accordingly, threshold excitation power, P_{th}, is defined as the power required for lasing upon excitation with $\lambda_{\text{in}} = \lambda_{p,0} + 5.4$ pm.

Figure 3(b) shows the results for higher P_{input}. The upper panel shows pump resonance spectra, and the lower panel represents SRE spectra. For a P_{input} of $2.0 \times P_{\text{th}}$, the intensity of the SRE spectrum continues to increase nonlinearly due to enhanced Raman gain. Consequently, the range of λ_{in} suitable for lasing ($\Delta\Lambda_{\text{lasing}}$) expands significantly, and even exceeds $\Delta\lambda_{p,0}$. On the other hand, intensity of the pump mode increases only by a factor of 1.2 between $1.1 \times P_{\text{th}}$ and $2.0 \times P_{\text{th}}$. This factor is too small even if we take the wavelength conversion by SRS into account, and therefore, the small increase indicates that pump photon density begins to saturate due to optical loss through TPA-induced FCA. For $P_{\text{input}} = 4.0 \times P_{\text{th}}$, the peak intensity of the SRE spectrum is slightly lower than that for $2.0 \times P_{\text{th}}$. This suggests that the loss via FCA is enhanced to a degree that it can compete with the Raman gain. On the other hand, $\Delta\Lambda_{\text{lasing}}$ still increases, and λ_{SRE} still coincides with λ_p. We also note that a dip appears in the SRE spectrum at 1424.017 nm. For a P_{input} of $8.0 \times P_{\text{th}}$, the shape of the SRE spectrum is quite different from that of the pump mode. Intensities at the long-wavelength region are significantly reduced, and the SRE peak appears at 1424.013 nm, which differs from λ_p (1424.028 nm). We confirmed that the decrease in intensity in the long-wavelength region is further enhanced for $P_{\text{input}} > 8.0 \times P_{\text{th}}$. On the other hand, $\Delta\Lambda_{\text{lasing}}$ continued to increase (see Fig. 5).

It is noted that $\Delta\Lambda_{\text{lasing}}$ for each P_{input} agrees well with the range where intensity of the pump emission is larger than the thin dashed line in the upper panel in Fig. 3(b). Therefore, we consider that the thin dashed line represents threshold pump intensity, $P_{\text{th,pump}}$, for the lasing. It is also noted that Raman laser intensity is significantly reduced in the region for long wavelengths and high P_{input}. This loss seems to appear and grow substantially after pump photon density exceeds a certain threshold value, $P_{\text{th,loss}}$ [thick dotted line in the upper panel in Fig. 3(b)]. The red shift of λ_p and increase of $\Delta\lambda_p$ due to the refractive index shift by TPA

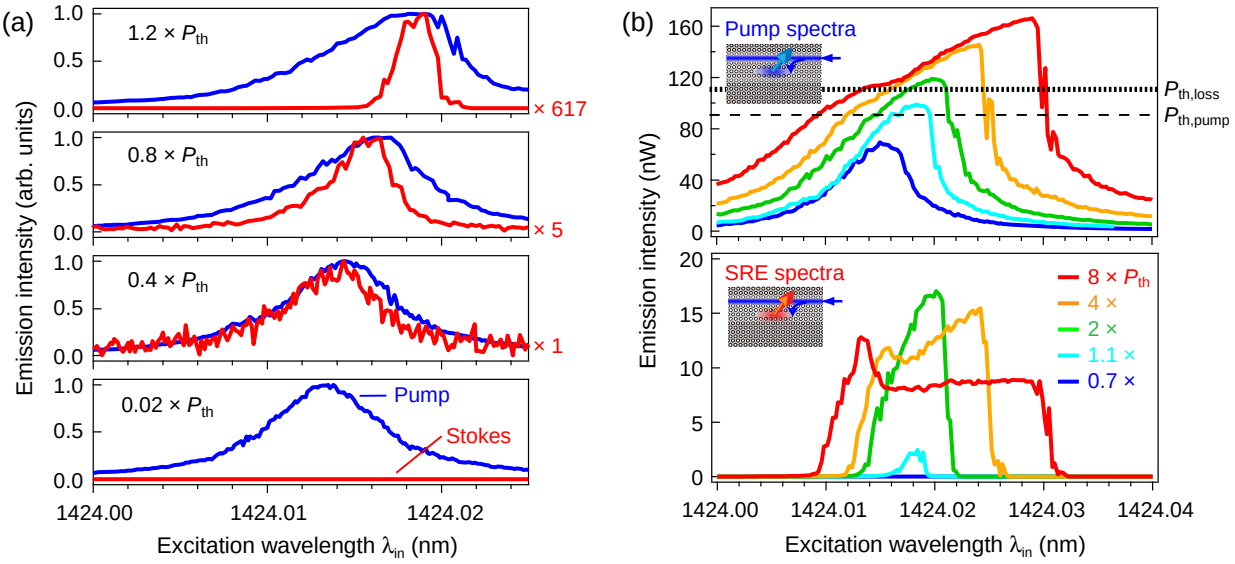

Fig. 3. (a) Resonance spectra for the pump nanocavity mode (blue curves) and SRE spectra (red curves) for $P_{\text{input}} \le 1.2 \times P_{\text{th}}$. (b) Resonance spectra for the pump mode (upper panel) and SRE spectra (lower panel) for $0.7 \times P_{\text{th}} \le P_{\text{input}} \le 8.0 \times P_{\text{th}}$. Emission intensities were measured by Ge photodiode sensor (Thorlabs S132C). Insets illustrate how the nanocavity modes were excited.

carriers continue for high P_{input}, though intensity of the pump mode does not increase that much. Therefore, we consider that the reduction of SRE intensity at the long-wavelength region originates from TPA. We confirmed similar trends for SRE spectra in samples with different Q and Δf. To increase laser output, the cause of this nonlinear intensity decrease in the SRE spectrum should be clarified.

B. Numerical Investigation of SRE Spectra

To interpret the abovementioned peculiar intensity reduction at the long-wavelength region, we perform a numerical simulation using coupled-mode theory [18]. Figure 4 shows the calculation results where the carrier-plasma effect, thermo-optic effect, and Kerr effect induced by TPA carriers are included. Details of the calculation method and original numerical data (comprising the time evolution of the number of photons in the two nanocavity modes, shifts of λ_p and λ_S, and free-carrier density N_C) employed to obtain these spectra are given in Section S2 of Supplement 1.

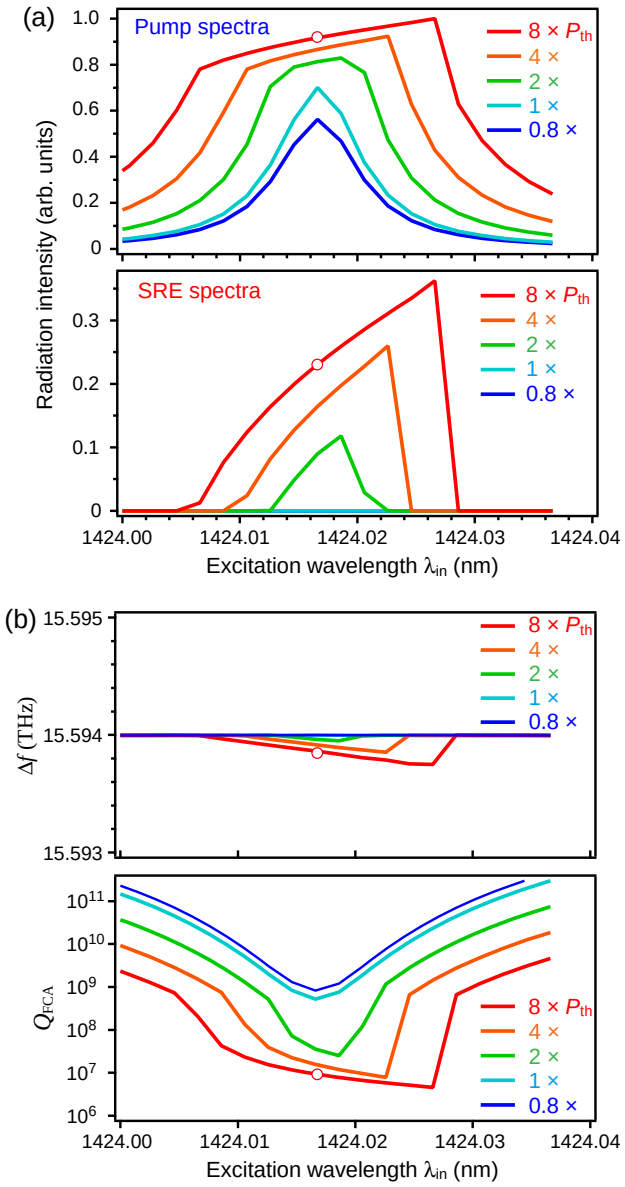

Fig. 4. (a) Calculated resonant emission spectra for the pump mode (upper panel) and Stokes mode (lower panel) for the range $0.8 \times P_{\text{th}} \le P_{\text{input}} \le 8.0 \times P_{\text{th}}$. (b) Corresponding shift in frequency spacing Δf (upper panel) and the change in Q_{FCA} (lower panel). The original numerical data for the points indicated by the open circles are presented in Fig. S4 of Supplement 1.

Figure 4(a) shows the calculated resonant emission spectra for the pump mode (upper panel) and Stokes mode (lower panel). The spectral shapes of the pump mode's resonant emission are in good agreement with experimental results, i.e., the red shift of λ_p, increase of $\Delta\lambda_p$, and saturation of emission are well reproduced. The shapes of the SRE spectra also agree with experimental results up to $2.0 \times P_{\text{th}}$ (although not visible for $1.0 \times P_{\text{th}}$). However, the reduction in SRE intensity at the long-wavelength region for higher P_{input} is not reproduced. Furthermore, we confirmed that the calculated λ_{SRE} coincides with λ_p for $P_{\text{input}} > 8.0 \times P_{\text{th}}$ and the calculated SRE intensities continue to increase.

The upper panel in Fig. 4(b) shows the λ_{in} dependence of Δf for various P_{input}. Although the TPA carriers also induce a dynamical shift of λ_S, the magnitude is similar to the TPA-induced shift of λ_p [see Fig. S4(b) in Supplement 1]. Accordingly, the shift for Δf is very small, more than two orders of magnitude smaller than the Raman gain width (approximately 0.08 THz) [43]. Therefore, the Δf shift is not detrimental for Raman lasing, and it is not a main cause for the nonlinear decrease in SRE intensity.

The lower panel in Fig. 4(b) shows the λ_{in} dependence of the additional Q factor due to the TPA-induced FCA (Q_{FCA}). A high Q_S is essential for Raman lasing [12], but it is decreased by FCA according to the following relation:

$$\frac{1}{Q_S} = \frac{1}{Q_{S,0}} + \frac{1}{Q_{\text{FCA}}}. \tag{2}$$

$Q_{S,0}$ is 1,290,000 for low P_{input}, as shown in Fig. 1(f). Q_{FCA} can be evaluated using [18,39]

$$Q_{\text{FCA}} = \frac{2\pi n}{N_C \sigma_{\text{FCA}} \lambda_S}, \tag{3}$$

where n is the refractive index, and the absorption cross section for FCA, σ_{FCA}, is 1.06×10^{-17} cm^2 [44]. In the range from $1.0 \times P_{\text{th}}$ to $2.0 \times P_{\text{th}}$, the magnitude of Q_{FCA} at λ_p rapidly decreases because the N_C rapidly increases above the threshold due to the high Q_S. It is noted that the Q_{FCA} at λ_p for $8.0 \times P_{\text{th}}$ is 4.5×10^6, which is much larger than the $Q_{S,0}$. In addition, the decrease in the Q_{FCA} tends to saturate for $P_{\text{input}} > 4.0 \times P_{\text{th}}$. Such a tendency has been observed in time-domain measurements for $P_{\text{input}} < 2.0 \times P_{\text{th}}$ (we experimentally estimated a Q_{FCA} for this region to be between 5.0×10^6 and 6.0×10^6 [18]). There is no conclusive evidence that the nonlinear loss $1/Q_{\text{FCA}}$ for the Stokes mode is actually responsible for the decrease in SRE intensity at the long-wavelength region.

We suspect that the increase in carrier lifetime for high P_{input} is responsible for the peculiar SRE behavior. It is known that Si nanocavities have short carrier lifetimes of about 1 ns due to the large ratio between surface area and volume of the cavity [45,46]. The lifetimes are more than 10 times shorter than those of cavities based on rib waveguides [13,14], which is a strong advantage for the nanocavity-based Raman Si laser. If almost all surface states that aid carrier recombination are occupied by TPA carriers, the carrier lifetime will increase, and as a result, loss via FCA, $1/Q_{\text{FCA}}$, might substantially increase. This mechanism

can drastically lower the Q_S in Eq. (2). $P_{th,loss}$ denoted in Fig. 3(b) may indicate such a boundary. If we employ a lateral p-i-n diode structure with the heterostructure nanocavity being located in the *i*-region while maintaining $Q_{S,0}$, the N_C can be reduced by applying a reverse bias [13,14,37]. A modification of the surface condition could also be an effective method to shorten carrier lifetime [42]. Both methods should increase the $P_{th,loss}$ value and thus improve laser output at high P_{input}.

C. SRE Image

Figure 5(a) shows the color plot of SRE intensity as a function of excitation wavelength (horizontal) and power (vertical). This image visually correlates all important laser characteristics, e.g., λ_{in} where laser oscillation starts, the excitation condition for maximum laser output, increase in $\Delta\Lambda_{lasing}$, and decrease in gain at the long-wavelength region.

Figure 5(b) shows $\Delta\Lambda_{lasing}$ and $\Delta\lambda_{SRE}$ as a function of P_{input}. $\Delta\Lambda_{lasing}$ is 1.5 pm at P_{th} and monotonically increases as P_{input} increases. It can be confirmed that $\Delta\Lambda_{lasing}$ exceeds $\Delta\lambda_{p,0}$ at $2.0 \times P_{th}$ and increases up to 30 pm at $12.0 \times P_{th}$. On the other hand, $\Delta\lambda_{SRE}$ begins to decrease above $8.0 \times P_{th}$ due to the increase in FCA loss in the long-wavelength region.

Figure 5(c) shows the change in λ_{SRE} relative to $\lambda_{p,0}$ for various P_{input}. Raman lasing starts at P_{th} with a peak wavelength of $\lambda_{p,0} + 5.4$ pm. As P_{input} is increased, λ_{SRE} monotonously red shifts until $P_{input} = 5.0 \times P_{th}$, which resembles the red shift observed for λ_p. At P_{input} of $6.0 \times P_{th}$, λ_{SRE} suddenly shifts from $\lambda_{p,0} + 13.0$ pm to $\lambda_{p,0} + 1.4$ pm due to the increase in FCA loss in the long-wavelength region. No further red shift of λ_{SRE} was observed for higher excitation powers.

Figure 5(d) shows the input–output characteristics for various fixed λ_{in}, which are indicated with dashed lines in Fig. 5(a). The green curve shows data for $\lambda_{in} = \lambda_{p,0} + 5.4$ pm, which has the lowest threshold. The red curve corresponds to data for $\lambda_{in} = \lambda_{p,0} + 8.4$ pm. Here, the largest intensity is obtained at $P_{input} = 2.5 \times P_{th}$. Although the green and the red curves exhibit a similar dependence on P_{input}, Raman laser intensity for excitation with $\lambda_{p,0} + 8.4$ pm becomes larger for $P_{input} > 2.0 \times P_{th}$ due to the red shift of λ_p. Both intensities decrease above $2.5 \times P_{th}$, which suggests that FCA loss increases more rapidly than Raman gain. The blue curve corresponds to $\lambda_{in} = \lambda_{p,0} + 1.4$ pm and exhibits the highest intensity in the region above $6.0 \times P_{th}$. The gray line represents intensity at the optimized λ_{SRE} for each P_{input}. It rapidly decreases between $2.5 \times P_{th}$ and $5.0 \times P_{th}$ due to FCA loss, and increases again for $P_{input} > 6.0 \times P_{th}$, since λ_{SRE} moves to the short-wavelength region.

The wavelength dependence of Raman gain including features of nonlinear optical losses has not been reported so far, but is revealed by SRE spectroscopy. Raman laser output and energy efficiency can be enhanced by reducing the nonlinear optical loss induced by TPA carriers. As can be seen in the SRE image, the variation of λ_{in} by several pm is able to induce or stop Raman laser oscillation. In other words, a small shift of λ_p by several pm is also able to induce or stop the lasing. Such a shift can be caused electrically by adding a p-i-n structure to the nanocavity [47]. Accordingly, realization of low-power-driven switching devices with an extinction ratio of larger than 30 dB should be possible

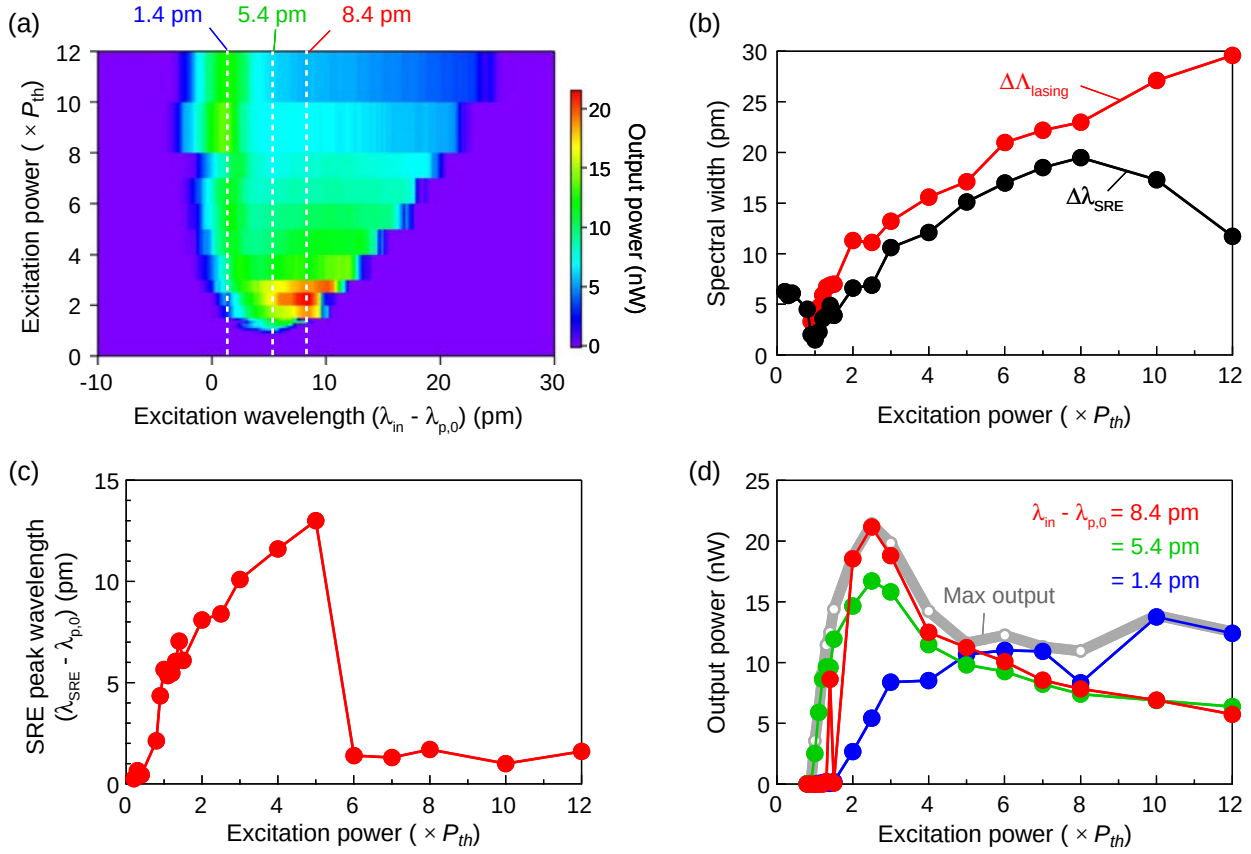

Fig. 5. (a) Color map of Raman laser output power versus P_{input} and λ_{in}. The horizontal axis plots the difference between excitation wavelengths λ_{in} and $\lambda_{p,0}$. (b) $\Delta\lambda_{SRE}$ and $\Delta\Lambda_{lasing}$ as a function of P_{input}. (c) λ_{SRE} as a function of P_{input} (relative to $\lambda_{p,0}$). (d) Raman laser output power characteristics for the three λ_{in} indicated in (a) as a function of P_{input}. The gray curve is the maximum obtainable output power.

by using Raman Si nanocavity lasers (see Fig. S2 in Supplement 1). The switching speed, however, is limited by the high-Q factors [18]. In general, a hysteresis response of the SRE spectrum with regard to the sweeping direction is possible because of the accumulation of heat generated by TPA carriers. No hysteresis was observed in this experiment since, we chopped the excitation laser light, as shown in Fig. 2 [30,31]. The hysteresis response is also useful for switching devices, and we confirmed that it appears upon placing the chopper in the collection path just before the photodiode (see Section S3 of Supplement 1).

5. CONCLUSION

In conclusion, we studied the excitation-wavelength dependence of optical gain in a high-Q nanocavity-based Raman Si laser by employing SRE spectroscopy and numerical simulations. SRE spectra can be used to clarify the gain mechanism below and above the threshold. The SRE image composed of several SRE spectra at different pump powers helps to understand the relation of all important laser characteristics. To improve laser output and efficiency, the nonlinear loss appearing in the long-wavelength region of SRE spectra should be reduced. We propose that the decrease in carrier lifetime is an important factor for performance improvements. We consider that the SRE spectroscopy presented here will be useful also for other types of Raman lasers based on different types of high-Q microcavities.

Funding. Japan Society for the Promotion of Science (JSPS) KAKENHI (15H05428, 18H01479); Toray Foundation; New Energy and Industrial Technology Development Organization (NEDO); Asahi Glass Foundation.

Acknowledgment. D. Y. was supported by the Program for Leading Graduate Schools and a research fellowship of the Japan Society for the Promotion of Science from the Ministry of Education, Culture, Sports, Science, and Technology in Japan (MEXT).

See Supplement 1 for supporting content.

REFERENCES

1. L. Pavesi, S. Gaponenko, and L. Dal Negro, *Towards the First Silicon Laser* (Kluwer Academic, 2003).
2. S. S. Iyer and Y.-H. Xie, "Light emission from silicon," Science **260**, 40–46 (1993).
3. R. Claps, D. Dimitropoulos, Y. Han, and B. Jalali, "Observation of Raman emission in silicon waveguides at 1.54 μm," Opt. Express **10**, 1305–1313 (2002).
4. R. Claps, D. Dimitropoulos, V. Raghunathan, Y. Han, and B. Jalali, "Observation of stimulated Raman amplification in silicon waveguides," Opt. Express **11**, 1731–1739 (2003).
5. R. Espinola, J. Dadap, R. Osgood, S. McNab, and Y. Vlasov, "Raman amplification in ultrasmall silicon-on-insulator wire waveguides," Opt. Express **12**, 3713–3718 (2004).
6. A. Liu, H. Rong, M. Paniccia, O. Cohen, and D. Hak, "Net optical gain in a low loss silicon-on-insulator waveguide by stimulated Raman scattering," Opt. Express **12**, 4261–4268 (2004).
7. Q. Xu, V. Almeida, and M. Lipson, "Time-resolved study of Raman gain in highly confined silicon-on-insulator waveguides," Opt. Express **12**, 4437–4442 (2004).
8. O. Boyraz and B. Jalali, "Demonstration of a silicon Raman laser," Opt. Express **12**, 5269–5273 (2004).
9. M. Krause, H. Renner, and E. Brinkmeyer, "Analysis of Raman lasing characteristics in silicon-on-insulator waveguides," Opt. Express **12**, 5703–5710 (2004).
10. T. Liang and H. Tsang, "Efficient Raman amplification in silicon-on-insulator waveguides," Appl. Phys. Lett. **85**, 3343–3345 (2004).
11. R. Jones, H. Rong, A. Liu, A. Fang, M. Paniccia, D. Hak, and O. Cohen, "Net continuous wave optical gain in a low loss silicon-on-insulator waveguide by stimulated Raman scattering," Opt. Express **13**, 519–525 (2005).
12. X. Yang and C. W. Wong, "Coupled-mode theory for stimulated Raman scattering in high-Q/Vm silicon photonic band gap defect cavity lasers," Opt. Express **15**, 4763–4780 (2007).
13. H. Rong, R. Jones, A. Liu, O. Cohen, D. Hak, A. Fang, and M. Paniccia, "A continuous-wave Raman silicon laser," Nature **433**, 725–728 (2005).
14. H. Rong, S. Xu, Y. Kuo, V. Sih, O. Cohen, O. Raday, and M. Paniccia, "Low-threshold continuous-wave Raman silicon laser," Nat. Photonics **1**, 232–237 (2007).
15. Y. Takahashi, Y. Inui, M. Chihara, T. Asano, R. Terawaki, and S. Noda, "A micrometre-scale Raman silicon laser with a microwatt threshold," Nature **498**, 470–474 (2013).
16. Y. Takahashi, Y. Inui, M. Chihara, T. Asano, R. Terawaki, and S. Noda, "High-Q resonant modes in a photonic crystal heterostructure nanocavity and applicability to a Raman silicon laser," Phys. Rev. B **88**, 235313 (2013).
17. D. Yamashita, Y. Takahashi, T. Asano, and S. Noda, "Raman shift and strain effect in high-Q photonic crystal silicon nanocavity," Opt. Express **23**, 3951–3959 (2015).
18. D. Yamashita, T. Asano, S. Noda, and Y. Takahashi, "Lasing dynamics of optically-pumped ultralow-threshold Raman silicon nanocavity lasers," Phys. Rev. Appl. **10**, 024039 (2018).
19. K. Ashida, M. Okano, M. Ohtsuka, M. Seki, N. Yokoyama, K. Koshino, M. Mori, T. Asano, S. Noda, and Y. Takahashi, "Ultrahigh-Q photonic crystal nanocavities fabricated by CMOS process technologies," Opt. Express **25**, 18165–18174 (2017).
20. K. Ashida, M. Okano, M. Ohtsuka, M. Seki, N. Yokoyama, K. Koshino, K. Yamada, and Y. Takahashi, "Photonic crystal nanocavities with an average Q factor of 1.9 million fabricated on a 300-mm-wide SOI wafer using a CMOS-compatible process," J. Lightwave Technol. **36**, 4774–4782 (2018).
21. P. J. Dean, "Energy-dependent capture cross sections and the photoluminescence excitation spectra of gallium phosphide above the threshold for intrinsic interband absorption," Phys. Rev. **168**, 889–901 (1968).
22. B. Monemar, "Fundamental energy gap of GaN from photoluminescence excitation spectra," Phys. Rev. B **10**, 676–681 (1974).
23. D. Hessman, P. Castrillo, M. E. Pistol, C. Pryor, and L. Samuelson, "Excited states of individual quantum dots studied by photoluminescence spectroscopy," Appl. Phys. Lett. **69**, 749–751 (1996).
24. H. Itoh, Y. Hayamizu, M. Yoshita, H. Akiyama, L. Pfeiffer, K. West, M. Szymanska, and P. Littlewood, "Polarization-dependent photoluminescence-excitation spectra of one-dimensional exciton and continuum states in T-shaped quantum wires," Appl. Phys. Lett. **83**, 2043–2045 (2003).
25. K. L. Shaklee and R. F. Leheny, "Direct determination of optical gain in semiconductor crystals," Appl. Phys. Lett. **18**, 475–477 (1971).
26. G. Mohs, T. Aoki, R. Shimano, M. Kuwata-Gonokami, and S. Nakamura, "On the gain mechanism in GaN based laser diodes," Solid State Commun. **108**, 105–109 (1998).
27. B. W. Hakki and T. L. Paoli, "Gain spectra in GaAs double-heterostructure injection lasers," J. Appl. Phys. **46**, 1299–1306 (1975).
28. D. T. Cassidy, "Technique for measurement of the gain spectra of semiconductor diode lasers," J. Appl. Phys. **56**, 3096–3099 (1984).
29. Y. Hayamizu, M. Yoshita, Y. Takahashi, H. Akiyama, C. Z. Ning, L. N. Pfeiffer, and K. W. West, "Biexciton gain and the Mott transition in GaAs quantum wires," Phys. Rev. Lett. **99**, 167403 (2007).
30. M. Notomi, A. Shinya, S. Mitsugi, G. Kira, E. Kuramochi, and T. Tanabe, "Optical bistable switching action of Si high-Q photonic-crystal nanocavities," Opt. Express **13**, 2678–2687 (2005).
31. T. Uesugi, B. S. Song, T. Asano, and S. Noda, "Investigation of optical nonlinearities in an ultra-high-Q Si nanocavity in a two-dimensional photonic crystal slab," Opt. Express **14**, 377–386 (2006).
32. T. Tanabe, H. Sumikura, H. Taniyama, A. Shinya, and M. Notomi, "All-silicon sub-Gb/s telecom detector with low dark current and high quantum efficiency on chip," Appl. Phys. Lett. **96**, 101103 (2010).
33. J. Yang, T. Gu, J. Zheng, M. Yu, G.-Q. Lo, D.-L. Kwong, and C. W. Wong, "Radio frequency regenerative oscillations in monolithic high-Q/V

heterostructured photonic crystal cavities," Appl. Phys. Lett. **104**, 061104 (2014).
34. T. Liang and H. Tsang, "Role of free carriers from two-photon absorption in Raman amplification in silicon-on-insulator waveguides," Appl. Phys. Lett. **84**, 2745–2747 (2004).
35. T. Liang and H. Tsang, "Nonlinear absorption and Raman scattering in silicon-on-insulator optical waveguides," IEEE J. Sel. Top. Quantum Electron. **10**, 1149–1153 (2004).
36. H. Rong, A. Liu, R. Nicolaescu, M. Paniccia, O. Cohen, and D. Hak, "Raman gain and nonlinear optical absorption measurements in a low-loss silicon waveguide," Appl. Phys. Lett. **85**, 2196–2198 (2004).
37. D. Dimitropoulos, R. Jhaveri, R. Claps, J. C. S. Woo, and B. Jalali, "Lifetime of photogenerated carriers in silicon-on-insulator rib waveguides," Appl. Phys. Lett. **86**, 071115 (2005).
38. B. S. Song, S. Noda, T. Asano, and Y. Akahane, "Ultra-high-Q photonic double-heterostructure nanocavity," Nat. Mater. **4**, 207–210 (2005).
39. T. Asano, B.-S. Song, and S. Noda, "Analysis of the experimental Q factors (~1 million) of photonic crystal nanocavities," Opt. Express **14**, 1996–2002 (2006).
40. H. Hagino, Y. Takahashi, Y. Tanaka, T. Asano, and S. Noda, "Effects of fluctuation in air hole radii and positions on optical characteristics in photonic crystal heterostructure nanocavities," Phys. Rev. B **79**, 085112 (2009).
41. H. Sekoguchi, Y. Takahashi, T. Asano, and S. Noda, "Photonic crystal nanocavity with a Q-factor of ~9 million," Opt. Express **22**, 916–924 (2014).
42. T. Asano, Y. Ochi, Y. Takahashi, K. Kishimoto, and S. Noda, "Photonic crystal nanocavity with a Q factor exceeding eleven million," Opt. Express **25**, 1769–1777 (2017).
43. V. Sih, S. Xu, Y.-H. Kuo, H. Rong, M. Paniccia, O. Cohen, and O. Raday, "Raman amplification of 40 Gb/s data in low-loss silicon waveguides," Opt. Express **15**, 357–362 (2007).
44. J. C. Sturm and C. M. Reaves, "Silicon temperature measurement by infrared absorption. Fundamental processes and doping effects," IEEE Trans. Electron Devices **39**, 81–88 (1992).
45. T. Tanabe, K. Nishiguchi, A. Shinya, E. Kuramochi, H. Inokawa, M. Notomi, K. Yamada, T. Tsuchizawa, T. Watanabe, H. Fukuda, H. Shinojima, and S. Itabashi, "Fast all-optical switching using ion-implanted silicon photonic crystal nanocavities," Appl. Phys. Lett. **90**, 031115 (2007).
46. M. Fujita, B. Gelloz, N. Koshida, and S. Noda, "Reduction in surface recombination and enhancement of light emission in silicon photonic crystals treated by high-pressure water-vapor annealing," Appl. Phys. Lett. **97**, 121111 (2010).
47. T. Tanabe, K. Nishiguchi, E. Kuramochi, and M. Notomi, "Low power and fast electro-optic silicon modulator with lateral p-i-n embedded photonic crystal nanocavity," Opt. Express **17**, 22505–22513 (2009).